Energy Storage Materials 44 (2022) 461–468

Contents lists available at ScienceDirect

Energy Storage Materials

journal homepage: www.elsevier.com/locate/ensm

Initial-anode-free aluminum ion batteries: In-depth monitoring and mechanism studies

Lei Wang[a,b,1], Xinmei Song[a,b,1], Yi Hu[a,b], Wen Yan[a,b], Zuoxiu Tie[a,b], Zhong Jin[a,b,*]

[a] MOE Key Laboratory of Mesoscopic Chemistry, MOE Key Laboratory of High Performance Polymer Materials and Technology, Jiangsu Key Laboratory of Advanced Organic Materials, School of Chemistry and Chemical Engineering, Nanjing University, Nanjing 210023, China
[b] Shenzhen Research Institute of Nanjing University, Shenzhen 518063, China

ARTICLE INFO

Key Words:
Multivalent-ion secondary batteries
Rechargeable aluminum-ion batteries
Electrochemical mechanisms
Initial-anode-free batteries
Anodic alternative materials

ABSTRACT

Rechargeable aluminum-ion batteries have attracted great attention due to the high theoretical volumetric capacity, good safety and abundant sources. Although tremendous efforts have been concentrated on exploring novel electrode materials for aluminum-ion batteries, the electrochemical mechanism still need to be further investigated. In this work, we found that even without employing any initial anode materials, the aluminum-ion batteries assembled with graphite cathode, $AlCl_3$/ion liquid based electrolyte and various anodic current collectors still can be stably charged/discharged. A variety of carbon or metal based materials can be utilized as anodic current collectors in the initial-anode-free aluminum-ion batteries; however, their anti-corrosion capabilities against Cl^- ions do greatly affect the battery performances. The electrochemical mechanism of initial-anode-free aluminum-ion batteries were comprehensively investigated by a series of *in-situ* and *ex-situ* spectroscopic and microscopic methods, revealing the reversible Al metal plating/stripping processes on the anodic current collectors during the charge-discharge cycles. We hope this work may provide new insights into the key component design and mechanism study of initial-anode-free multivalent secondary batteries.

1. Introduction

Exploiting novel rechargeable battery systems with high operation safety and environmental benignity is of great importance for the sustainable development of our society [1,2]. Rechargeable aluminum-ion batteries (AIBs) have attracted broad attention due to the nature abundance of Al, the nonflammability of $AlCl_3$/ionic liquid (IL) based electrolyte and the high theoretical specific capacity of three-electron redox processes [3]. Great efforts have been made to screen high-performance cathode materials for AIBs, such as metal chalcogenides [4–13], MXenes [14], conducting polymers [15–17] and carbon-based materials [3,18–21]. Although the ion intercalation/de-intercalation processes on the cathode side of AIBs and the choices of cathodic current collectors [22–24] have been studied by *ex-situ* X-ray diffraction (XRD) and Raman spectroscopy [3,21], the electrochemical behavior on the anode side is still to be comprehensively investigated. On the other hand, interestingly and strangely, it is normally assumed that the presence of Al metal foil on the anode side is a necessity for AIBs, but this assertion is unfounded.

In this work, we assembled AIBs by coupling commercial graphite paper (GP) cathode with $AlCl_3$/[EMIm]Cl electrolyte and various anodic current collectors (ACCs), such as GP, Mo, Cu, Ag, Ni, stainless steel (SS304) and Mg foils. Free of Al metal anode, the AIBs still can be stably charged/discharged. However, the electrochemical performances of AIBs based on different ACCs show great differences. The electrochemically stable ACCs, such as GP and Mo foils, exhibit good cycling stability and high Coulombic efficiencies (CE) comparable to Al anode. In contrast, the metallic ACCs susceptible to the corrosion of Cl^- ions, such as Cu, Ag, Ni, steel and Mg foils, exhibit relatively low specific capacities or rapid capacity fade rates during long-term cycling tests. To further investigate the detailed working mechanism of the initial-anode-free AIBs, a series of *in-situ* and *ex-situ* spectroscopic characterizations were systematically conducted. On the cathodic side, *in-situ* Raman and XRD analyses verified the reversible intercalation/de-intercalation of $AlCl_4^-$ anions into/from the GP interlayers during the charge-discharge processes, consistent with previous literature [3]. Unexpectedly, on the anodic side, *ex-situ* XRD, X-ray photoelectron spectroscopy (XPS), transmission electron microscopy (TEM), high-resolution transmission elec-

* Corresponding author at: MOE Key Laboratory of Mesoscopic Chemistry, MOE Key Laboratory of High Performance Polymer Materials and Technology, Jiangsu Key Laboratory of Advanced Organic Materials, School of Chemistry and Chemical Engineering, Nanjing University, Nanjing 210023, China.
E-mail address: zhongjin@nju.edu.cn (Z. Jin).
[1] These authors contributed equally to this work.

https://doi.org/10.1016/j.ensm.2021.10.044
Received 25 August 2021; Received in revised form 18 October 2021; Accepted 31 October 2021
Available online 3 November 2021

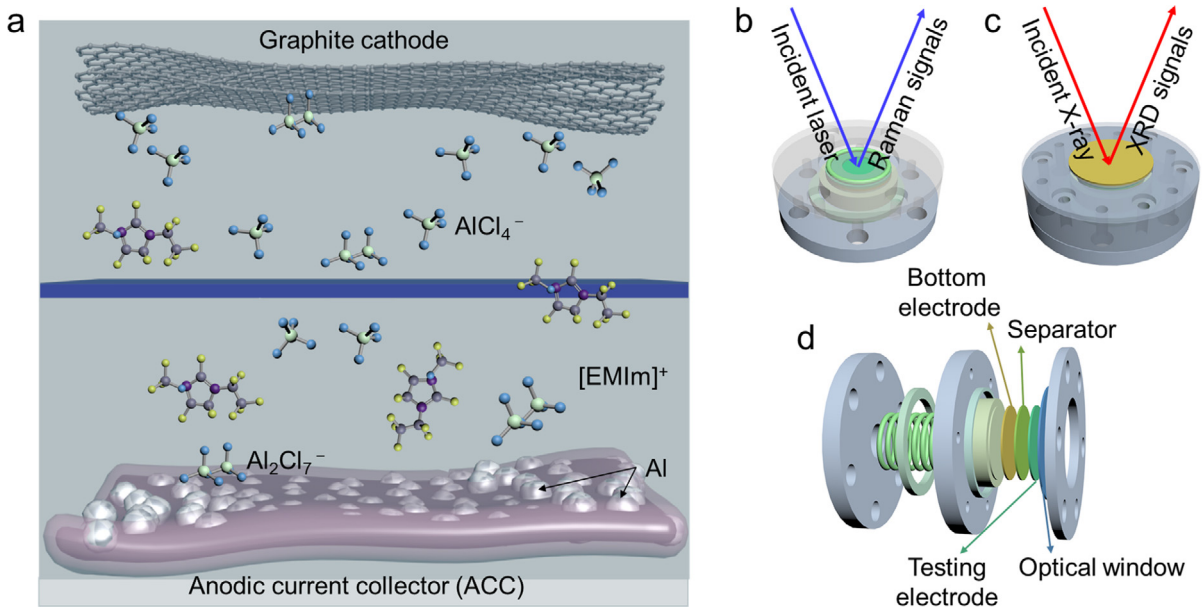

Fig. 1. Schematic structure and *in-situ* characterization system for the initial-anode-free AIBs. a Schematic drawing of the initial-anode-free AIBs based on GP cathodes and various ACCs. **b, c** Schematic cell setups used for **b** *in-situ* Raman and **c** *in-situ* XRD characterizations of AIBs. **d** The internal structure of the *in-situ* characterization cell setups in **b** and **c**.

tron microscopy (HRTEM), Auger electron spectroscopy (AES), scanning electron microscopy (SEM) and X-ray energy dispersive spectroscopy (EDS) mapping confirmed the reversible plating/stripping of Al metal on the surface of ACCs during cycling, no matter what the material of ACC was used. This is to say, the ACCs on the anodic side of AIBs just played an essential role as a substrate for Al metal plating/stripping. Interestingly, the initial-anode-free AIBs based on different ACC materials showed great differences on the electrochemical performances. To further understand the reasons of this phenomenon, a series of *ex-situ* characterizations of the ACCs at different charge/discharge states were conducted. It revealed that the anti-corrosion capabilities of ACC materials against Cl^- ions presented strong influences on the battery performances. For the ACC materials with high chemical stability in the $AlCl_3$/[EMIm]Cl electrolyte, such as GP and Mo foils, there was almost no surface corrosion observed after long-term cycling. However, for the other ACC martials less resistant to the corrosion of Cl^- anions, such as Cu, Ag, Ni, steel and Mg foils, the surfaces of these ACCs were proved to be corroded to different extents after cycling, indicating the occurrence of side reactions resulted in rapid capacity fading. According to the experimental results, we conclude that carbon or metal based materials with high anti-corrosion capability to Cl^- ions can serve as favorable ACC materials for the construction of initial-anode-free AIBs. In this work, the intriguing concept of initial-anode-free AIBs was proposed and the detailed working mechanism was comprehensively studied, throw light on the unique operation principle and tremendous application potential of initial-anode-free AIBs.

2. Results and discussion

To demonstrate the proof-of-concept, the coin cells of AIBs were constructed by using commercial GP as both the cathode material and cathodic current collector (**Fig. S1**), meanwhile the mixture of anhydrous $AlCl_3$ and 1-Ethyl-3-methylimidazolium chloride ([EMIm]Cl) IL was used as the electrolyte. For the construction of conventional AIBs, high-purity Al foil was used as the anode material; Alternatively, for the construction of initial-anode-free AIBs, various of graphitic- or metallic-materials (including GP, Mo, Cu, Ag, Ni, steel and Mg foils) were attempted to serve as the ACCs, as illustrated in Fig. 1**a**. To investigate the working mechanism on the cathodic side, we conducted *in-situ* Raman and XRD analyses for verifying the intercalation/de-intercalation behavior of choloraluminate ($AlCl_4^-$) anions into/from GP cathode. The external and inertial structures of the cell apparatus for *in-situ* Raman and XRD measurements are depicted in Fig. 1**b–d**. In these *in-situ* cells, the incident laser or X-ray entered into the quartz or beryllium (Be) windows, and then the Raman or XRD signals ejected out and finally detected by corresponding charge-coupled devices (CCD), respectively. To study the electrochemical processes on the anodic side, we also performed *in-situ* Raman and XRD analyses on GP ACC, verifying that there is no ion intercalation/de-intercalation behavior on the GP ACC. Moreover, *ex-situ* XPS, TEM, HRTEM and AES were also carried out to reveal the Al plating/stripping processes onto/from the GP ACC during charging/discharging. As for the various metallic ACCs (including Mo, Cu, Ag, Ni, steel and Mg foils), *ex-situ* XRD and EDS were conducted to prove the similar mechanism of Al plating/stripping processes compared to that of GP ACC. Furthermore, to clarify the occurrence of surface corrosion phenomena among some of the metallic ACCs during cycling, *ex-situ* SEM, EDS and XPS were implemented. Except Mo ACC, it was verified that the Cu, Ag, Ni, steel and Mg ACCs were corroded by $AlCl_3$/[EMIm]Cl electrolyte during cycling, leading to inferior electrochemical performances of the corresponding AIBs.

The electrochemical performances of the AIBs based on Al anode or various ACCs were firstly analyzed by CV measurements. Fig. 2**a** displayed the CV curves of AIBs based on GP ACC. In the 1st anodic scan, a strong oxidation peak emerged at ~2.22 V, which was attributed to the intercalation of $AlCl_4^-$ into the GP interlayers on the cathode side. During the subsequent scans, this peak was slightly shifted to 2.19 V. The backward scan curves were relatively complicated, exhibited a dominated reduction peak at ~1.67 V during the 1st cycle and then shifted to ~1.73 V in the subsequent scans, which might come from the formation of a solid-electrolyte interface (SEI) on the GP surface. Apart from the peak located at ~1.67 V, four shoulder peaks were observed at about 2.21, 2.04, 1.00 and 0.70 V, respectively, which were assigned to the step-by-step stages of the de-intercalation of $AlCl_4^-$ ions into the GP cathode [25]. The CV curves of AIBs based on Al anodes or various ACCs (Mo, Cu, Ag, Ni, steel and Mg) are shown in **Fig. S2**. The CV results of AIBs based on Al anode or Mo, Cu, Ni and steel ACCs are similar to that of the AIBs based on GP ACC, indicating the similar electrochemical behavior of these AIBs. However, the CV curves of

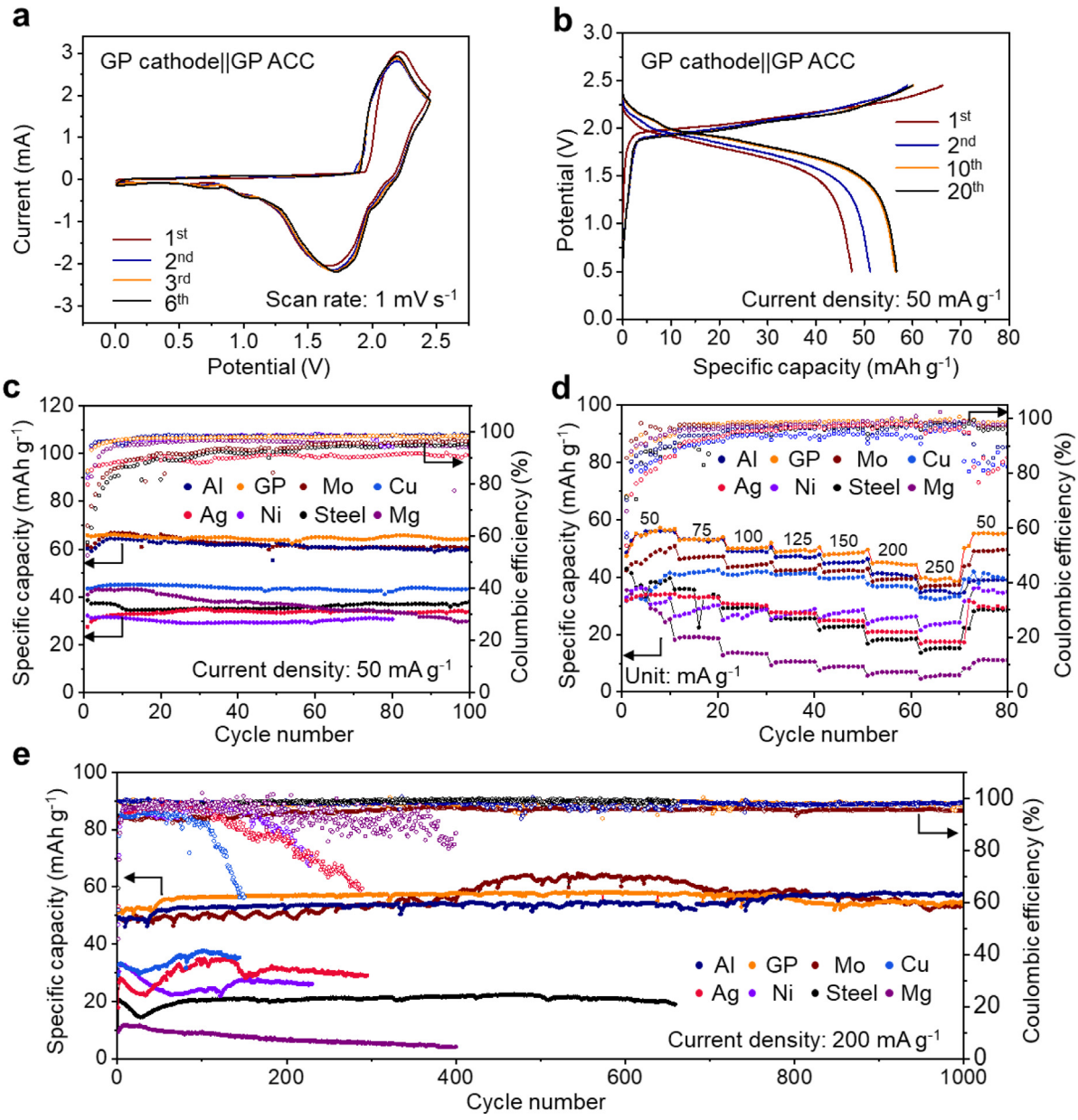

Fig. 2. Electrochemical measurements of the AIBs. a Cyclic voltammetry (CV) curves of the initial-anode-free AIBs based on GP ACC. **b** Galvanostatic charge-discharge voltage profiles of the initial-anode-free AIBs based on GP ACC at 50 mA g^{-1}. **c** Cycling performances of the AIBs based on Al anode or various ACCs. **d** Rate performance and **e** long-term cycling performance of the AIBs based on Al anode or various ACCs. The specific capacity data of AIBs were all recorded between a voltage range of 0.5–2.45 V.

AIBs based on Ag and Mg ACCs were quite different from those of other AIBs, suggesting the occurrence of intensive side reactions induced by Cl^- corrosion to Ag an Mg metals, which will be detailedly discussed in the following section. The galvanostatic charge-discharge curves of AIBs based on GP ACC at a current density of 50 mA g^{-1} are depicted in Fig. 2**b**. The two plateaus centering at approximately 2.20 and 1.80 V indicated the de-intercalation from the GP cathode during the discharge processes [18]. In this work, the values of all specific capacities were calculated based on the loading mass of GP cathode, and the amounts of used $AlCl_3$/[EMIm]Cl electrolyte were excessive. The cycling performances of AIBs based on Al anode or various ACCs at 50 mA g^{-1} are shown in Fig. 2**c**. During the 100 cycles, the AIBs based on Al anode exhibited a well-maintained specific capacity of ~62.0 mAh g^{-1} and a high average CE of ~99.2%. Competitively, the AIBs based on GP and Mo ACCs also displayed high cycling stability, showing similar specific capacities (65.1 and 61.5 mAh g^{-1}) and relatively high CE values (98.7% and 96.6%), respectively. However, the AIBs based on Cu, Ag, Ni, steel and Mg ACCs exhibited much lower specific capacities and relatively low CE values, which shall be ascribed to the electrochemical corrosion of these ACCs by $AlCl_3$/[EMIm]Cl electrolyte. Specifically, during the Al metal plating/stripping processes on different ACCs, the irreversible occurrence of side reactions between electrolyte and Cu, Ag, Ni, steel and Mg ACCs could lead to serious consumption of the electrolyte and then the electrolyte even become the insufficient component in these AIB systems, thus greatly limiting the specific capacities.

The rate performances of these AIBs are also measured, as shown in Fig. 2**d**. At a relatively high current density of 250 mA g^{-1}, the AIBs based on Al anode still delivered a specific capacity of 35.2 mAh g^{-1}, and the discharge capacity returned to 53.4 mAh g^{-1} when the current density was recovered to 50 mA g^{-1}. Similarly, the AIBs based on GP and

Mo ACCs cycled at 250 mA g^{-1} exhibited reversible specific capacities with comparable values (39.6 and 37.4 mA h g^{-1}, respectively); When the current density decreased to 50 mA g^{-1}, the specific capacities could recover to 55.9 and 50.4 mA h g^{-1}, respectively, indicating the good rate performances of initial-anode-free AIBs based on GP and Mo ACCs. By contrast, the AIBs with Cu, Ag, Ni, steel and Mg ACCs showed much inferior rate performances compared to those with GP and Mo ACCs (**Fig. 2d**).

The long-term cycling performances of the AIBs at 200 mA g^{-1} are also depicted in **Fig. 2e**. The AIBs based on Al anode showed a discharge capacity of 58.0 mAh g^{-1} and a high average CE of 98.6% after ~1000 cycles. Similarly, The AIBs based on GP and Mo ACCs delivered well-maintained discharge capacities (54.6 and 53.2 mAh g^{-1}) and high CE values (98.1% and 95.8%) after ~1000 cycles, respectively, representing their good cycling stability. Nevertheless, the AIBs based on Cu, Ag, Ni, steel and Mg ACCs suffered from inferior cycling stability or low CE values. Moreover, the initial CE values of the AIBs based on Al anode or GP and Mo ACCs were as high as 98.9%, 98.7% and 92.1%, respectively, and could maintain a high level in the following cycles, indicating the good anti-corrosion capability to Cl^- ions of these three materials. It could be concluded that both GP and Mo foils are good choices of ACC materials in initial-anode-free AIBs, attributing to their high electrochemical stability to serve as favourable substrates for Al plating/stripping. By contrast, the initial CE values of the AIBs based on Cu, Ag, Ni, steel and Mg ACCs were significantly inferior (57.2%, 58.5%, 51.5%, 65.5% and 46.0%, respectively), revealing that the occurrence of side reactions between the metal and the electrolyte, resulting in irreversible changes during the charge-discharge cycles. In the first 100 cycles, the CE values of the AIBs based on Cu, Ag, Ni and Mg ACCs still could be maintained at ~95% even through there are trace side reactions. However, during the subsequent charge-discharge processes after 100 cycles, when the irreversible changes accumulated to a certain extent, the CE curves showed significant drops accompanied by the failure of the cells. Distinctively, although the initial CE values of the AIBs based on steel ACC was low, the CE increased to above 98% in the subsequent cycles and showed no downward trend for more than 600 cycles. This result suggests the formation of a passivation layer on the surface of steel ACC during the initial cycles, which could effectively prevent the metal from further irreversible corrosion of Cl^- ions.

To avoid the peak shifting in Raman and XRD spectra of the sample upon exposure to air, we performed *in-situ* characterizations for improving the reliability and repeatability of the spectroscopic analyses. The *in-situ* Raman spectra of GP cathode at various charge-discharge states during the 2nd cycle is shown in **Fig. 3a**. The G band of pristine GP cathode was presented at around 1584 cm^{-1}. As the charge voltage increased to 2.00 V, the G band of GP cathode slightly blue-shifted and split into two peaks, E_{2g2}(i) mode (1586 cm^{-1}) and E_{2g2}(b) mode (1607 cm^{-1}). The E_{2g2}(i) mode was ascribed to the vibrations of carbon atoms in the interior of GP layer planes (not adjacent to intercalated layer planes), and the high-wavenumber E_{2g2}(b) mode was attributed to the vibrations of carbon atoms in bonded GP layers (adjacent to the intercalated layer planes). The presence of E_{2g2}(i) mode and E_{2g2}(b) mode confirmed the intercalation of $AlCl_4^-$ anions into GP. When the charge voltage further increased to 2.45 V, the E_{2g2}(i) mode gradually weakened and disappeared, and the E_{2g2}(b) mode was enhanced and blue-shifted to 1622 cm^{-1}, indicating the saturated intercalation of $AlCl_4^-$ anions. During the subsequent discharge process from 2.45 to 1.80 V, the E_{2g2}(b) mode moved back to 1612 cm^{-1} and the E_{2g2}(i) mode emerged again. When the discharge voltage further decreased from 1.80 to 0.50 V, the intensity of E_{2g2}(i) mode increased and the intensity of E_{2g2}(b) mode decreased. These two modes red-shifted and merged into a broad shoulder peak (G band), indicating the de-intercalation of $AlCl_4^-$ anions from GP cathode, which is in consistent with the reported literature [18]. Notably, the Raman signal variations in the 3rd and 4th cycles (**Fig. S3**) were similar to those in the 2nd cycle (**Fig. 3a**), proving the good reversibility of the intercalation/de-intercalation of $AlCl_4^-$ into/from GP interlayers. The *in-situ* Raman signals of the $AlCl_3$/[EMIm]Cl electrolyte on the surface of GP cathode are displayed in **Fig. 3b**. As detailed in **Fig. S4**, the peaks located at 174 and 310 cm^{-1} were assigned to $Al_2Cl_7^-$ anions, and the peaks at around 339, 369, 487 and 583 cm^{-1} were associated with $AlCl_4^-$, $[EMIm]^+$, $AlCl_2^+$ and $[AlCl_2{\bullet}([EMIm]Cl)]^+$, respectively [3]. The chloroaluminate intercalation was evident from the intensity increase of $AlCl_4^-$ signal while charging and its subsequent intensity decrease while discharging. The *in-situ* XRD patterns of GP cathode are shown in **Fig. 3c**. During the charge process, beside the original (002) peak of GP at 26.58° (d ~ 3.37 Å), two additional diffraction peaks emerged at around 23.37° (d ~ 3.84 Å) and 27.96° (d ~ 3.20 Å), revealing the interlayer distance variations induced by the $AlCl_4^-$ anions intercalation [3]. Upon discharging, these two peaks gradually vanished, and only a single (002) peak at 26.60° (d ~ 3.37 Å) was remained when the cell was discharged to 0.50 V. Importantly, there is nearly no position shift of the (002) peak after a charge-discharge cycle, indicating the high lattice stability of GP cathode. Moreover, the *ex-situ* XPS spectra at Al 2p and Cl 2p regions of GP cathode were also collected at pristine, fully-charged and fully-discharged states, as shown in **Fig. S5**. The peak intensities of Al and Cl species obviously increased at fully-charged state while substantially reduced at fully-discharged state, verifying that the $AlCl_4^-$ anions were reversibly intercalated/de-intercalated into/from the GP cathode.

The function mechanism of GP ACC was also investigated by various *in-situ* and *ex-situ* characterizations. **Fig. 3d** displays the *in-situ* Raman spectra of $AlCl_3$/[EMIm]Cl electrolyte on the surface of GP ACC during the 2nd cycle. As summarized in **Fig. S6**, the peaks centered at 177 and 310 cm^{-1} were assigned to $Al_2Cl_7^-$ anions, and the peaks at 345 and 589 cm^{-1} were attributed to $AlCl_4^-$ and $[AlCl_2{\bullet}([EMIm]Cl)]^+$, respectively. Compared to **Fig. S4**, the slight deviations of Raman peak positions were caused by the change of the chemical environment. The characteristic peak of $[AlCl_2{\bullet}([EMIm]Cl)]^+$ cations decreased while charging and then recovered back while discharging, owing to the participation and concentration variation of $AlCl_2{\bullet}([EMIm]Cl)]^+$ cations during the Al plating/stripping processes on GP ACC. Notably, the *in-situ* XRD patterns of GP ACC at the (002) diffraction peak region of GP (20−30°) show almost no change during the charge-discharge processes (**Fig. S7**), indicating that there is no ion intercalation/de-intercalation occurred in the GP ACC. **Fig. 3e** and its inset display typical TEM and HRTEM images of the GP ACC at fully-charged state, respectively. Clear Al (111) lattice planes were observed from the HRTEM image, suggesting the presence of Al electro-plating/stripping behavior on the GP ACC. Moreover, as shown in the wide-region XRD patterns of the GP ACC at fully-charged state (**Fig. 3f**), the diffraction peaks corresponding to the (111) and (200) planes of metal Al particles were emerged at 38.7° and 43.4°, respectively, confirming the Al plating/stripping mechanisms on GP ACC. **Fig. 3g** shows the Al_{2p} XPS profiles of the GP ACC at fully-charged state etched by Ar-ion bombardment for different durations. The peak located at 72.8 eV was attributed to the metal Al. The Al 2p peak still existed even after the Ar-ion etching for 25 min, indicating the abundant electro-deposition of Al metal during the charge process. The AES image and corresponding elemental mappings of a GP ACC at fully-charged state after 20 min of Ar-ion etching are shown in **Fig. 4h, i**. The relatively weak Auger signals of C and the strong Auger signals of Al indicated the electro-plating of Al metal on the surface of GP ACC. The remaining Auger signals of Cl species were attributed to the trapped/adsorbed electrolyte on GP ACC. Moreover, **Fig. 4j** exhibited the Al_{KLL} AES profiles of a GP ACC at fully-charged state after different Ar-ion etching durations. The kinetic energy of Al_{KLL} shifted from 1384.6 eV to 1382.7 eV after Ar-ion etching for 20 min, proving the formation of metal Al on GP ACC while charging.

Corresponding to the above results, the redox reactions in the AIBs based on GP cathode and Al anode or various ACCs in the charge-discharge processes can be written as:

$$\text{Cathode}: C_n + AlCl_4^- \rightleftharpoons C_n[AlCl_4] + e^- \quad (1)$$

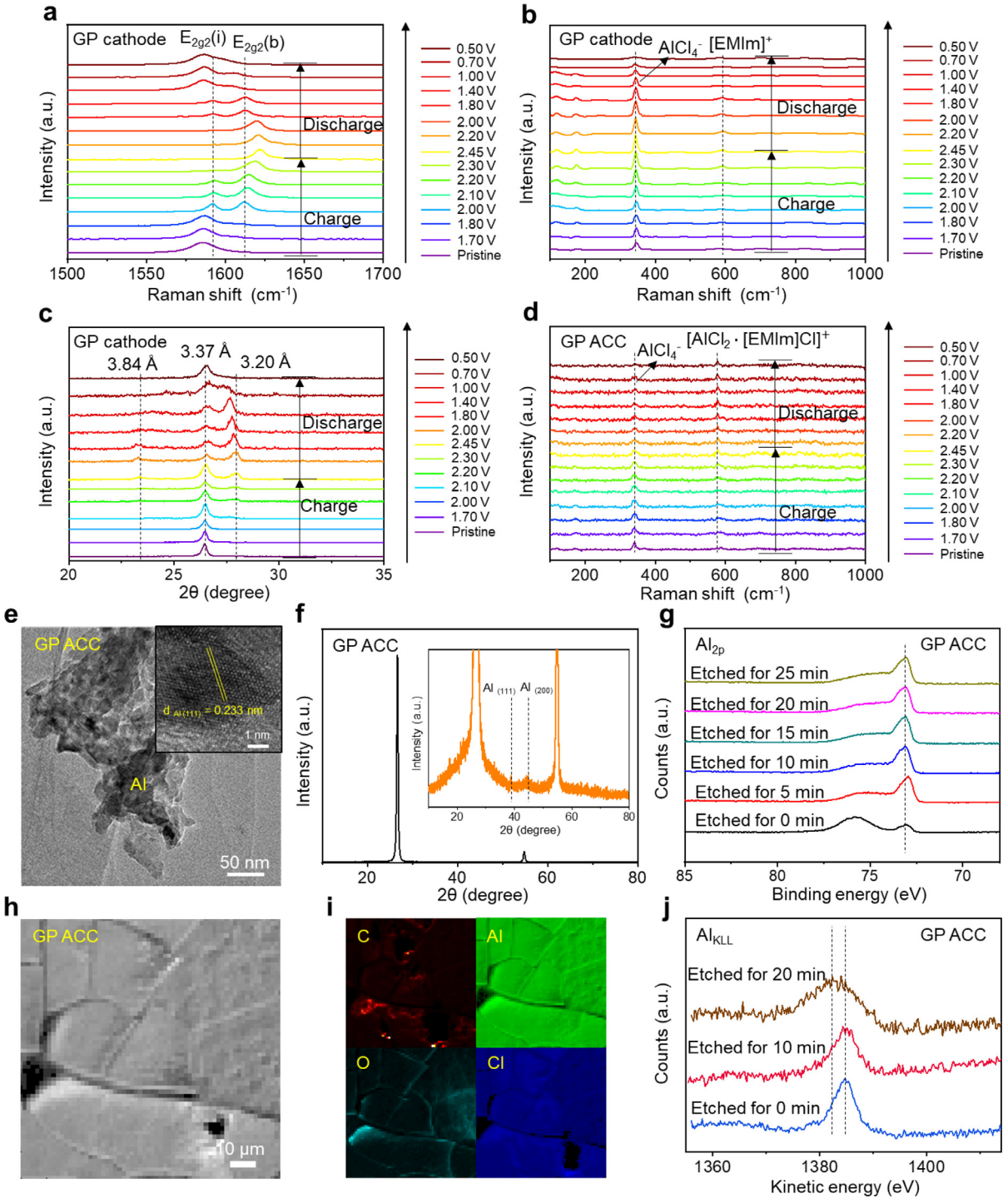

Fig. 3. ***In-situ*** **and** ***ex-situ*** **characterizations of the AIBs based on GP cathode and GP ACC. a, b** *In-situ* Raman spectra recorded on GP cathode, showing the Raman signals of **a** the GP cathode and **b** the $AlCl_3$/[EMIm]Cl electrolyte on the surface of GP cathode during the 2nd cycle, respectively. **c** *In-situ* XRD patterns of the GP cathode during the 2nd cycle. **d** *In-situ* Raman spectra recorded on GP ACC, showing the Raman signals of $AlCl_3$/[EMIm]Cl electrolyte on the surface of GP ACC during the 2nd cycle. **e** TEM image of GP ACC at fully-charged state. The inset shows a HRTEM image of a metal Al particle electro-plated on GP ACC during the charging process. **f** XRD patterns of GP ACC at fully-charged state, showing the diffraction peaks of metal Al particles electro-plated on GP ACC during the charging process. **g** XPS Al_{2p} spectra of GP ACC at fully-charged state etched by argon ion bombardment for 0, 5, 10, 15, 20 and 25 min, respectively. **h** AES image and **i** corresponding AES elemental mappings of GP ACC at fully-charged state etched by argon ion bombardment for 20 min. **j** The Al_{KLL} AES profiles of GP ACC at fully-charged state etched by argon ion bombardment for 0, 10 and 20 min, respectively.

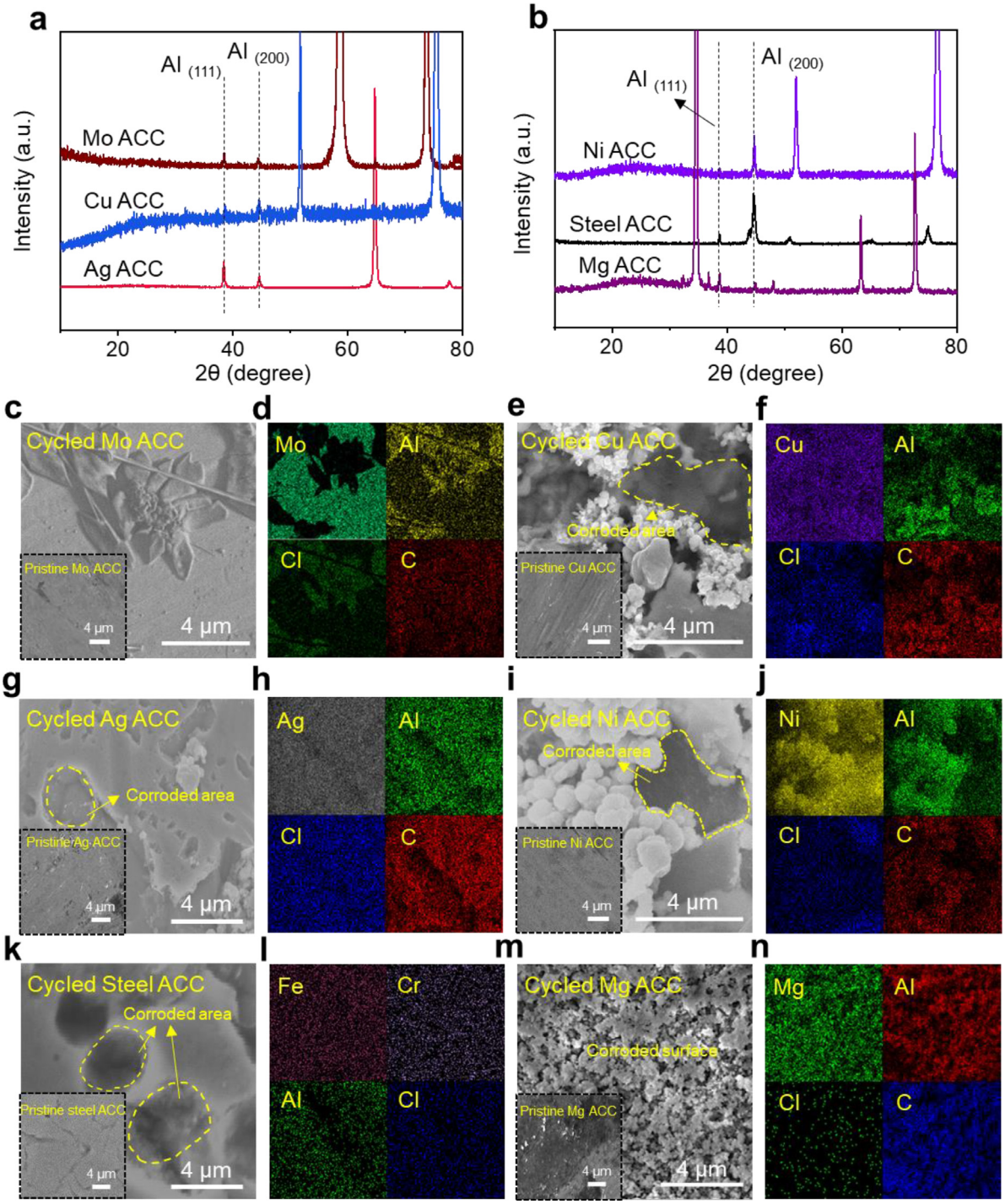

Fig. 4. ***Ex-situ*** **characterizations of Mo, Cu, Ag, Ni, steel and Mg ACCs. a, b** *Ex-situ* XRD patterns of Mo, Cu, Ag, Ni, steel and Mg ACCs at fully-charged state after 100 cycles 50 mA g^{-1}, respectively. **c–n** SEM images and corresponding EDS elemental mappings of Mo, Cu, Ag, Ni, steel and Mg ACCs at fully-discharged state after 100 cycles 50 mA g^{-1}, respectively.

"

$$\text{Anode}: AlCl_2{\cdot}EMImCl^{+} + 2Al_2Cl_7^{-} + 3e^{-} \rightleftharpoons Al + 4AlCl_4^{-} + [EMIm]Cl \quad (2)$$

where n is the number of carbon atoms involved for the intercalation of each $AlCl_4^-$ anion in the GP cathode. In this work, n is calculated to be 34, according to the experimental results in Fig. 2**c**, which is about one third higher than the theoretical prediction in previous literature [26], following a general trend of secondary batteries that the experimental capacities are normally lower than the theoretical maximum capacities.

To explore the working mechanism and surface corrosion degree of Mo, Cu, Ag, Ni, steel and Mg ACCs in initial-anode-free AIBs, *ex-situ* XRD, SEM, EDS and XPS characterizations have been comprehensively conducted. The XRD patterns of various metallic ACCs at fully-charged state are shown in Fig. 4**a, b**. Two new diffraction peaks corresponding to the (111) and (200) planes of metal Al were emerged at 38.7° and 43.4°, respectively, further verifying the electro-deposition of metal Al particles during the charge processes. To inquire the surface morphologies and anti-corrosion properties of these ACCs in AIBs, *ex-situ* SEM and EDS analyses were performed before and after 100 cycles at a current density of 50 mA g^{-1} (Fig. 4**c–n** and **Fig. S8**). Specifically, the Mo ACC at fully-discharged state presented a smooth surface mor-

phology without recognizable signs of corrosion (Fig. 4**c, d**), indicating its good anti-corrosion performance and high electrochemical stability in AIBs. In contrast, the Cu, Ni, Ag and steel ACCs exhibited uneven and rough surfaces as pointed out by the areas outlined with yellow dash lines (Fig. 4**e–k**), revealing the side reactions and surface corrosions triggered by the Cl^--containing electrolyte during cycling, which resulted in relatively low capacity, inferior CE and poor cycling life. Notably, the unusual high content of Cl element (23%) on Ag ACC at fully-charged state is in sharp contrast to those of Mo, Cu, Ni, steel and Mg ACCs, as revealed by EDS analysis (**Fig. S8**), indicating the formation of AgCl on the surface of Ag ACC. XPS analysis was further conducted to investigate the compositions and chemical states of the substances on the surface of Ag ACC at fully-charged state (**Fig. S9**). In the Ag 3d XPS spectrum (**Fig. S9a**), two sharp peaks at around 367.44 eV and 373.47 eV were assignable to Ag $3d_{3/2}$ and Ag $3d_{5/2}$ bands belonging to Ag^+ species [27], verifying the formation of AgCl during cycling, which led to the poor electrochemical performances of Ag ACC based AIBs. Moreover, the Al 2p XPS spectrum of Ag ACC at fully-charged state exhibited a strong peak at around 72.8 eV corresponding to metal Al (**Fig. S9b**), further confirming the electro-plating/stripping of Al, which was consistent with the *ex-situ* XRD result (Fig. 4**a**). The SEM image and corresponding EDS elemental mappings of Mg ACC at fully-discharged state (Fig. 4**m, n**) revealed that the entire surface was very rough due to the Cl^- corrosion. At fully-charged state, the rugged surface of Mg ACC was covered by Mg- and Al-containing components (**Fig. S10**), confirming the electro-plating of metal Al on the corroded Mg ACC. To further explore the corrosion degree of Mg ACC, cross-section SEM characterization and EDS elemental mappings of Mg ACC at fully-charged state were carried out, as shown in **Fig. S11**. The lumpy morphology and the presence of Al species on the surface of Mg ACC confirmed the etching of Mg ACC by $AlCl_3$/[EMIm]Cl electrolyte during cycling, which is the main reason resulted in the inferior cycling stability of the Mg ACC based AIBs.

3. Conclusion

In summary, here we present the proofs-of-concept of initial-anode-free AIBs consisted of GP cathode, $AlCl_3$/IL electrolyte and various types of ACCs without the necessity to employ any initial anode materials. The crucial function of the carbon or metal based ACCs is to serve as a substrate for electrochemical plating/stripping of metal Al. To comprehensively understand the working mechanisms of initial-anode-free AIBs, a series of *in-situ* and *ex-situ* spectroscopic and microscopic analyses were conducted. The systematic characterization results indicated that the charge/discharge processes were based on the $AlCl_4^-$ intercalation /deintercalation into/from the GP interlayers on the cathodic side and the plating/stripping of metal Al particles on the anodic side, respectively. However, the anti-corrosion capabilities of the ACCs against Cl^- ions do greatly influence the electrochemical performances of the AIBs. The GP and Mo foils were verified to be favourable choices of ACC materials for initial-anode-free AIBs, exhibiting high CE values and cycling stability owing to their high anti-corrosion capability in $AlCl_3$/IL electrolyte. On the contrary, Cu, Ag, Ni, steel and Mg foils led to inferior electrochemical performances because of their vulnerability against the corrosion of Cl^- ions to varying degrees. This work provides a helpful guide on the mechanism understanding and key component screening of initial-anode-free secondary batteries.

4. Methods

4.1. Chemicals and materials

Anhydrous aluminum chloride (99.985%) was purchased from Alfa Aesar. 1-Ethyl-3-methylimidazolium chloride ([EMIm]Cl) (99.0%) was purchased from Macklin Biochemical Co. Ltd. Commercial GP (50 μm thickness) was purchased from Jinglong Special Carbon Co. Ltd. Al foils (0.1 mm thickness, 99.99%) and Mo foils (0.02 mm thickness, 99.99%) were purchased from Zhicheng Metal Co. Ltd. Cu foils (0.05 mm thickness, 99.99%) were purchased from ShunXingwang Materials Co. Ltd. Ag foils (0.02 mm thickness, 99.999%) were purchased from Xinye Materials Co. Ltd. Ni foils (0.01 mm thickness, 99.99%) were purchased from Xingye Experiment Co. Ltd. Stainless steel (SS304, 0.2 mm thickness) foils were purchased from TianChenghe Experiment Co. Ltd. Mg foils (0.05 mm thickness, 99.99%) were purchased from Huabei Magnesium Co. Ltd (Hebei, China). All the chemicals and materials were used directly without further purification.

4.2. Preparation of GP electrodes

Briefly, commercial GP with 50 μm thickness was calcined in Ar flow (50 sccm) at 1000 °C for 3 h to remove residual moisture and unfavorable functional groups on the surface. After cooling to room temperature, the GP electrodes were stored in an Ar-filled glovebox ($[O_2]$ < 0.1 ppm, $[H_2O]$ < 0.1 ppm) for further use.

4.3. Preparation of $AlCl_3$/[EMIm]Cl electrolyte

Briefly, 1-Ethyl-3-methylimidazolium chloride ([EMIm]Cl) and anhydrous aluminum chloride ($AlCl_3$) were mixed with a molar ratio of 1.3:1 in an Ar-filled glovebox, and then stirred for 2 h to obtain the resulting IL electrolyte.

4.4. Electrochemical measurements

The 2032-type coin cell was constructed by using GP cathode and 40 μL of $AlCl_3$/[EMIm]Cl electrolyte. An additional Mo foil with a diameter of 19 mm was placed between the cathode and the stainless-steel cell shell to prevent the IL electrolyte from corroding the cell shell. On the anodic side, Al foil with a diameter of 14 mm was used as anode for the construction of conventional AIBs; Alternatively, various other materials (including GP Mo, Cu, Ag, Ni, steel and Mg) with a diameter of 14 mm were used as ACCs for the construction of initial-anode-free AIBs. Glassy fiber membrane (Whatman GF/D) was placed between the cathode and the anode (or ACC) as separator. The CV curves of AIBs were tested with a Chenhua CHI-760e electrochemical workstation. The galvanostatic discharge-charge curves and rate performance of AIBs were measured on a multichannel battery test system (Wuhan LAND CT2001A). The GP electrode discs with a diameter of 14 mm has an average mass of ~10 mg. The active materials mass of all batteries was set 10 mg and therefore the batteries gave a mass loading of active material was ~6.50 mg cm^{-2}.

4.5. In-situ *and* ex-situ *characterizations*

A field-emission scanning electron microscope (FESEM, FEI Nova NanoSEM 450) coupled with an X-ray energy dispersive spectroscope (EDS, Burker X-flash 6|30) and a transmission electron microscope (TEM, JEOL JEM-2100F) were used to analyze the morphological and compositional features of the electrode materials. *In-situ* Raman spectroscopy was performed on a Horiba HR Evolution Raman spectrometer coupled by an *in-situ* Raman characterization cell (with a quartz optical window, as shown in Fig. 1**b, d**) source during charge-discharge cycles at the current density of 80 mA g^{-1}. To avoid the possible influence of photoluminescence, a laser source of 473 nm wavelength length (blue) was used to excite the Raman signals. *In-situ* XRD measurements were conducted on a Shimadzu LabX XRD-6000 with a Cu Kα radiation (λ = 1.54178 Å) coupled by an *in-situ* XRD characterization cell (with a beryllium window) during charge-discharge cycles at 80 mA g^{-1}. The height of *in-situ* cell was aligned by the characteristic (002) peak of pristine graphite located about 26.38° After acquirement, the calculation might the adjust the (002) peak position to 26.38° by minus the offset. For *ex-situ* XPS and AES characterizations, the electrode was charged

or discharged to designated voltages. The cell was disassembled in an Ar-filled glovebox and the electrode was washed with methanol three times to remove the residual electrolyte. Then the electrode was quickly transferred in to the vacuum chamber of a PHI-5000 VersaProbe III X-ray photoelectron spectrometer for both e*x-situ* XPS and AES analyses by using an Al Kα X-ray source coupled with an Ar-ion etching/bombardment apparatus (Eqs. (1), (2)).

Declaration of Competing Interest

None.

Acknowledgments

This work was supported by the National Key Research and Development Program of China (2017YFA0208200), the Fundamental Research Funds for the Central Universities of China (0205–14380266), the National Natural Science Foundation of China (22022505, 21872069), the Natural Science Foundation of Jiangsu Province (BK20180008), and the Shenzhen Fundamental Research Program of Science, Technology and Innovation Commission of Shenzhen Municipality (JCYJ20180307155007589).

Supplementary materials

Supplementary material associated with this article can be found, in the online version, at doi:10.1016/j.ensm.2021.10.044.

References

[1] Y. Zhang, S. Liu, Y. Ji, J. Ma, H. Yu, Emerging nonaqueous aluminum-ion batteries: challenges, status, and perspectives, Adv. Mater. 30 (2018) 1706310.
[2] S. Das, Graphene: a cathode material of choice for aluminum-ion battery, Angew. Chem. Int. Ed. 57 (2018) 16606–16617.
[3] M. Lin, M. Gong, B. Lu, Y. Wu, D. Wang, M. Guan, M. Angell, C. Chen, J. Yang, B. Hwang, H Dai, An ultrafast rechargeable aluminium-ion battery, Nature 520 (2015) 325–328.
[4] N. Jayaprakash, S.K. Das, L.A Archer, The rechargeable aluminum-ion battery, Chem. Commun. 47 (2011) 12610.
[5] W. Kaveevivitchai, A. Huq, S. Wang, M.J. Park, A. Manthiram, Rechargeable aluminum-ion batteries based on an open-tunnel framework, Small 13 (2017) 1701296.
[6] J. Tu, H. Lei, Z. Yu, S. Jiao, Ordered WO3-x nanorods: facile synthesis and their electrochemical properties for aluminum-ion batteries, Chem. Commun. 54 (2018) 1343–1346.
[7] X. Zhang, G. Zhang, S. Wang, S. Li, S Jiao, Porous CuO microsphere architectures as high-performance cathode materials for aluminum-ion batteries, J. Mater. Chem. A 6 (2018) 3084–3090.
[8] L. Wang, H. Lin, W. Kong, Y. Hu, R. Chen, P. Zhao, M. Shokouhimehr, X. Zhang, Z. Tie, Z. Jin, Controlled growth and ion intercalation mechanism of monocrystalline niobium pentoxide nanotubes for advanced rechargeable aluminum-ion batteries, Nanoscale 12 (2020) 12531–12540.
[9] K. Liang, L. Ju, S. Koul, A. Kushima, Y Yang, Self-supported tin sulfide porous films for flexible aluminum-ion batteries, Adv. Energy. Mater. 9 (2019) 1802543.
[10] Y. Hu, D. Ye, B. Luo, H. Hu, X. Zhu, S. Wang, L. Li, S. Peng, L Wang, A binder-free and free-standing cobalt sulfide@carbon nanotube cathode material for aluminum-ion batteries, Adv. Mater. 30 (2018) 1703824.
[11] Z. Li, B. Niu, J. Liu, J. Li, F. Kang, A rechargeable aluminum-ion battery based on MoS_2 microsphere cathode, ACS Appl. Mater. Interfaces 10 (2018) 9451–9459.
[12] T. Cai, L. Zhao, H. Hu, T. Li, X. Li, S. Guo, Y. Li, Q. Xue, W. Xing, Z. Yan, L. Wang, Stable $CoSe_2$/carbon nanodice@reduced graphene oxide composites for high-performance rechargeable aluminum-ion batteries, Energy Environ. Sci. 11 (2018) 2341–2347.
[13] J. Jiang, H. Li, T. Fu, B. Hwang, X. Li, J. Zhao, One-dimensional Cu_2-xSe nanorods as cathode material for high-performance aluminum ion battery, ACS Appl. Mater. Interfaces 10 (2018) 17942–17949.
[14] A. Vahidmohammadi, A. Hadjikhani, S. Shahbazmohamadi, M. Beidaghi, Two-dimensional vanadium carbide (MXene) as a high capacity cathode material for rechargeable aluminum batteries, ACS Nano 11 (2017) 11135–11144.
[15] P.G. Pickup, R.A Osteryoung, Electrochemical polymerization of pyrrole and electrochemistry of polypyrrole films in ambient temperature molten salts, J. Am. Chem. Soc. 106 (1984) 2294–2299.
[16] L.M. Goldenberg, R.A. Osteryoung, Benzene polymerization in 1-ethyl-3-methylimidazolium chloride-$AlCl_3$, ionic liquid, Synth. Met. 64 (1994) 63–68.
[17] N.S. Hudak, Chloroaluminate-doped conducting polymers as positive electrodes in rechargeable aluminum batteries, J. Phys. Chem. C 118 (2014) 5203–5215.
[18] D. Wang, C. Wei, M. Lin, C. Pan, H. Chou, H. Chen, M. Gong, Y. Wu, C. Yuan, M. Angell, Y. Hsieh, Y. Chen, C. Wen, C. Chen, B.J. Hwang, C. Chen, H Dai, Advanced rechargeable aluminium ion battery with a high-quality natural graphite cathode, Nat. Commun. 8 (2017) 14283.
[19] Y. Wu, M. Gong, M. Lin, C. Yuan, M. Angell, L. Huang, D. Wang, V. Zhang, J. Yang, B. Hwang, H. Dai, 3D graphitic foams derived from chloroaluminate anion intercalation for ultrafast aluminum-ion battery, Adv. Mater. 28 (2016) 9218–9222.
[20] X. Yu, B. Wang, D. Gong, Z. Xu, B. Lu, Graphene nanoribbons on highly porous 3D graphene for high-capacity and ultrastable Al-ion batteries, Adv. Mater. 29 (2017) 1604118.
[21] H. Chen, F. Guo, Y. Liu, T. Huang, B. Zheng, N. Ananth, Z. Xu, W. Gao, Chao Gao, A defect-free principle for advanced graphene cathode of aluminum-ion battery, Adv. Mater. 29 (2017) 1605958.
[22] J. Shi, J. Zhang, J Guo, Avoiding pitfalls in rechargeable aluminum batteries research, ACS Energy Lett. 4 (2019) 2124–2129.
[23] Y. Oh, G. Lee, Y. Tak, Front cover: stability of metallic current collectors in acidic ionic liquid for rechargeable aluminum-ion batteries, ChemElectroChem 5 (2018) 1–6.
[24] L. Homen, D Shyamal, Active role of inactive current collector in aqueous aluminum-ion battery, Ionics (Kiel) 24 (2018) 2175–2180.
[25] P. Bhauriyal, A. Mahata, B. Pathak, The staging mechanism of AlCl4- intercalation in a graphite electrode for an aluminium-ion battery, Phys. Chem. Chem. Phys. 19 (2017) 7980–7989.
[26] S. Jung, Y. Kang, D. Yoo, J. Choi, Y Han, Flexible few-layered graphene for the ultrafast rechargeable aluminum-ion battery, J. Phys. Chem. C. 120 (2016) 13384–13389.
[27] Z. Ruan, G. Liu, J. Shu, C. Ren, Z Wang, Green synthesis of a AgCl@AgI nanocomposite using Laminaria japonica extract and its application as a visible-light-driven photocatalyst, RSC Adv. 9 (2019) 5858–5864.